JOURNAL OF THERMOPHYSICS AND HEAT TRANSFER
Vol. 10, No. 2, April–June 1996

Viscous Shock-Layer Study of Thermochemical Nonequilibrium

Roop N. Gupta*
NASA Langley Research Center, Hampton, Virginia 23681-0001

A two-temperature, viscous shock-layer (VSL) technique to analyze low-density (slip) effects and vibrational and electronic nonequilibrium for an 11-species airflow is presented. This formulation employs recently developed physical models, detailed transport and thermodynamic properties, and body and shock-slip conditions for multicomponent mixtures. Presently obtained results reproduce examined reentry flight data and numerical calculations with a good degree of accuracy over a wide range of conditions, validating its use for the calculation of low-to-high density flows. Detailed stagnation-region calculations along the trajectory of a proposed single-stage-to-orbit vehicle show significant vibrational and electronic nonequilibrium and slip effects at the highest considered altitude of 85 km. The combined effects of thermal nonequilibrium and slip lower the stagnation-point heating by about 24% at this altitude. These effects are negligible on surface quantities at 55 km altitude. At this altitude, however, the chemical nonequilibrium effects lower the stagnation heating obtained from chemical equilibrium calculations by about 21% for the Shuttle-like surface. The results provided here demonstrate the use of the VSL technique as a fast calculation procedure in a conceptual and preliminary design process, requiring sensitivity analysis and rapid reanalysis.

Nomenclature

C_i = mass fraction of species i, ρ_i/ρ
C_p = frozen specific heat of mixture at constant pressure, $C_{p,tr} + C_{p,ve}$
$C^i_{p,tr}$ = translational–rotational specific heat of species i at constant pressure, $C^{i*}_{p,tr}/C^*_{p,\infty}$
$C^i_{p,ve}$ = vibrational–electronic–electron specific heat of species i at constant pressure, $C^{i*}_{p,ve}/C^*_{p,\infty}$
$C^i_{v,ve}$ = vibrational–electronic–electron specific heat of species i at constant volume, $C^{i*}_{v,ve}/C^*_{p,\infty}$
$\hat{c}_1$ = fraction of the vibrational energy loss in dissociation
$\hat{D}_i$ = average vibrational energy per unit mass of molecule i, which is created or destroyed at rate $\dot{w}_i$, $\hat{D}^*_i/U^{*2}_\infty$
D_{ij} = binary diffusion coefficient for species i and j, $D^*_{ij}/(\mu^*_{\text{ref}}/\rho^*_\infty)$
D_{im} = effective diffusion coefficient for species i in mixture, $D^*_{im}/(\mu^*_{\text{ref}}/\rho^*_\infty)$
h = enthalpy of mixture $\Sigma\, C_i h_i$
h_i = enthalpy of species i, $h_{tr,i} + h_{ve,i}$
$h_{tr,i}$ = translational–rotational enthalpy of species i, $h^*_{tr,i}/U^{*2}_\infty$
$h_{ve,i}$ = vibrational–electronic–electron enthalpy of species i, $h^*_{ve,i}/U^{*2}_\infty$
I_i = first ionization energy of species i, $I^*_i/U^{*2}_\infty M^*_i$
K_{total} = frozen thermal conductivity of mixture, $K_{tr} + K_{ve}$
k^* = Boltzmann's constant, 1.38066×10^{-16} erg/K
$k^*_{f,r}$ = forward reaction-rate coefficient for reaction r, cm^3/mole-s
M_∞ = freestream Mach number
$\bar{M}^*$ = molecular weight of mixture, g/g-mole
M^*_i = molecular weight of species i, g/g-mole
N_s = number of reacting species
n = coordinate measured normal to the body n^*/R^*_N
n^*_i = number density of species i, particles/cm^3
p = pressure, $p^*/\rho^*_\infty U^{*2}_\infty$
p_e = electron pressure, $p^*_e/\rho^*_\infty U^{*2}_\infty$
q^*_r = radiative wall heat transfer rate, W/cm^2
q^*_T = total wall heat transfer rate, $q^*_w + \bar{\alpha} q^*_r$, W/cm^2
q_w = convective wall heat transfer rate, $q^*_w/\rho^*_\infty U^{*3}_\infty$
R^* = universal (molar) gas constant, 1.987 cal/g-mole-K
Re_∞ = freestream Reynolds number
R^*_i = gas constant for species i, R^*/M^*_i, cal/g-K
R^*_N = nose radius, cm
r = radius of the body surface, r^*/R^*_N
s = coordinate measured along the body surface, s^*/R^*_N
T = translational–rotational temperature, T^*/T^*_{ref}
T^*_{ref} = freestream reference temperature, $U^{*2}_\infty/C^*_{p,\infty}$
$\tilde{T}^*_{\text{ref}}$ = reference temperature for thermodynamic relations, 298.15 K
T_{ve} = vibrational–electronic–electron excitation temperature, $T^*_{ve}/T^*_{\text{ref}}$
U^*_∞ = freestream velocity, cm/s
u = velocity component tangent to body surface, u^*/U^*_∞
v = velocity component normal to body surface, v^*/U^*_∞
x_i = mole fraction of species i
$\bar{\alpha}$ = absorptance
γ = ratio of specific heats
$(\Delta h^{f*}_i)_{\tilde{T}^*_{\text{ref}}}$ = heat of formation of species i at temperature $\tilde{T}^*_{\text{ref}}$, cal/g-mole
ε = Reynolds number parameter, $\sqrt{\mu^*_{\text{ref}}/\rho^*_\infty U^*_\infty R^*_N}$
$\bar{\varepsilon}$ = char emissivity, Eq. (18)
κ = body curvature, $\kappa^* R^*_N$
μ = viscosity of mixture, μ^*/μ^*_{ref}
μ^*_{ref} = reference viscosity, $\mu^*(T^*_{\text{ref}})$, g/cm-s

Received Aug. 2, 1995; revision received Nov. 27, 1995; accepted for publication Nov. 30, 1995.

*Senior Research Engineer, Aerothermodynamics Branch, Gas Dynamics Division, Associate Fellow AIAA.

$\nu_{e,i}$ = collision frequency for electrons and heavy particles in electronic–translational ($e-T$) energy relaxation, $\nu^*_{e,i}/(U^*_\infty/R^*_N)$
ρ = density of mixture, ρ^*/ρ^*_∞
ρ_i = density of species i, ρ^*_i/ρ^*_∞
ρ^*_∞ = freestream density, g/cm^3
σ^* = Stefan–Boltzmann constant, 5.67×10^{-5} erg/cm^2-K^4-s

Subscripts
e = electronic mode; electrons
i, j, q = species indices
s = edge of Knudsen-layer value
sh = shock value
w = wall value
∞ = freestream value

Superscripts
i = species index
mol = molecule
s = edge of Knudsen-layer value
sh = shock value
w = wall value
$*$ = dimensional quantity
∞ = freestream value

Introduction

CURRENT and future plans for reusable transatmospheric vehicles and space exploration missions[1] will require sustained and maneuvering hypersonic flight at high altitudes where thermochemical nonequilibrium in the flowfield around a vehicle becomes significant. Lunar and other planetary missions will utilize the high-altitude atmosphere for aerobraking. Single-stage-to-orbit[1,2] (SSTO) and other next-generation transatmospheric vehicles will also traverse through upper parts of the Earth's atmosphere. Because of insufficient molecular collisions at high altitudes, chemical as well as thermal nonequilibrium (TNE) conditions will prevail in the shock layer surrounding such vehicles. Under thermal nonequilibrium conditions, a single temperature cannot be used to characterize the energy in translational, rotational, vibrational, and electronic modes of the gas. Compared to the thermal equilibrium (TE) state, the onset of ionization is enhanced and dissociation is diminished.[3] These thermal nonequilibrium effects compete and may play a significant role in the total heating load experienced by the transatmospheric vehicles.

Several investigators[3–6] have analyzed flowfields with thermochemical nonequilibrium by using the Navier–Stokes equations in conservative variables. Some results have also been presented[7] from a coupled radiation and Navier–Stokes calculation. Reference 8 provides results from a coupled radiation and viscous shock-layer calculation, mostly for the stagnation streamline of spherical nose bodies.

References 3, 4, 6, and 7 have provided results from a two-temperature model, whereas Refs. 5 and 8 have considered a three-temperature model. In the two-temperature model, one temperature T describes the distribution of heavy-particle translational and rotational energies, and a second temperature T_{ve} describes the distribution of vibrational, electronic, and electron translational energies. In the three-temperature model, nonequilibrium may exist between the vibrational energy and the electronic and electron energy, and separate temperatures are used to describe the distribution of energies in these two modes. Since considerable uncertainty exists in the models available for vibrational–electronic–electron energy relaxation, a two-temperature model appears reasonable. A two-temperature analysis also allows for a computationally more tractable and efficient formulartion of reacting flows with thermal nonequilibrium.

Results from a two-temperature viscous shock-layer formulation for flows around a body are provided in Refs. 9 and 10. Both of these formulations, however, employ the thin shock-layer assumption and are for vibrational nonequilibrium only under the assumption of a small degree of ionization in the shock layer. Also, both references have neglected chemical–vibrational coupling. That is, the effect of vibrational temperature on the reaction rate constants is not accounted for.

Since the transport and thermodynamic properties, reaction rates, various relaxation processes, and thermal radiation require various temperatures involved to evaluate them, it appears natural to formulate the energy equations in terms of different temperatures rather than specific energy/specific enthalpy or total enthalpy. This formulation also saves considerable computer time in avoiding a Newton–Raphson type iterative procedure of evaluating various temperatures from the specific energy or enthalpy. For design-oriented optimization techniques, requiring sensitivity analysis and rapid reanalysis, a fast calculation procedure of the type presented here is desirable.

In the present work, two energy equations are solved for the translational–rotational and vibrational–electronic–electron temperatures. Air chemistry is modeled according to Ref. 11. A modified Arrhenius expression is used for the forward- and backward-rate coefficients as shown in Table 1 of Ref. 12. Chemical–vibrational coupling is taken into account through the preferential dissociation and recombination model proposed by Park.[13]

Results obtained in the present study are compared with the flight data and some of the existing numerical values for reentry flows under thermal nonequilibrium conditions. Detailed calculations have been carried out for the nose region of a proposed SSTO vehicle[2] along an assumed entry trajectory given in Table 1. These calculations are intended to demonstrate the use of the viscous shock-layer (VSL) technique as a fast method to evaluate vibrational and electronic nonequilibrium along the trajectory of a flight vehicle. The inclusion of body and shock-slip boundary conditions in the VSL method makes it accurate with complete physics required for evaluating the low-to-high density flowfields encountered along such a trajectory.

Analysis

This section provides a brief description of the flow governing equations for a viscous compressible fluid in thermochemical nonequilibrium. Also given are descriptions of the thermodynamic and transport properties, chemical kinetics model with chemical–vibrational coupling, relaxation processes for the vibrational–translational and electronic–electron–translational energies, and body and shock-slip boundary conditions.

Table 1 Trajectory conditions and effective body parameters for a proposed SSTO vehicle[a]

Case	Time, s	Altitude, km	U^*_∞, km/s	ρ^*_∞, kg/m^3	ρ^*_∞, atm	T^*_∞, K	Re_∞	ε or $1/\sqrt{Re_{ref}}$	Mach. no.	Angle of attack
1	292	85	7.84	8.209×10^{-6}	4.394×10^{-6}	189	7,020	0.064	28.45	32.0
2	782	75	7.09	3.993×10^{-5}	2.357×10^{-5}	208	28,430	0.029	24.49	32.0
3	1,222	65	5.70	1.641×10^{-4}	1.085×10^{-4}	233	85,440	0.014	18.63	32.0
4	1,497	55	3.81	5.675×10^{-4}	4.192×10^{-4}	261	180,220	0.008	11.77	32.0

[a]Equivalent θ and R^*_N are 32 deg and 1.38 m, respectively. Freestream mole fractions are $x_{N_2} = 0.783$ and $x_{O_2} = 0.217$.

Flow Governing Equations

The viscous shock-layer equations are employed here for the flowfield analysis. These equations are obtained from the full Navier–Stokes equations by keeping terms up to second order in the inverse square root of the Reynolds number in both viscous and inviscid regions. This process results in one set of equations, unlike the boundary-layer equations, uniformly valid throughout the shock layer from moderately low to very large Reynolds numbers. The full viscous shock-layer equations in a body-oriented coordinate system for a multicomponent gas mixture in chemical nonequilibrium and thermal equilibrium are provided in Ref. 14. For a mixture in chemical and thermal nonequilibrium, the global continuity, tangential and normal momentum equations, and the species continuity equations (for the 11 air species N, O, N_2, O_2, NO, N^+, O^+, N_2^+, O_2^+, NO^+, and e^-) are the same as those given in Ref. 14. The two energy equations for a two-temperature (translational–rotational and vibrational–electronic–electron) model without radiation and the equation of state are given here.

Total energy (temperature) equation:

$$\rho C_{p,tr}\left(\frac{u}{1+n\kappa}\frac{\partial T}{\partial s}+v\frac{\partial T}{\partial n}\right)+\rho C_{p,ve}\times\left(\frac{u}{1+n\kappa}\frac{\partial T_{ve}}{\partial s}+v\frac{\partial T_{ve}}{\partial n}\right)-\left(\frac{u}{1+n\kappa}\frac{\partial p}{\partial s}+v\frac{\partial p}{\partial n}\right)=\varepsilon^2\left[\frac{\partial}{\partial n}\left(K_{tr}\frac{\partial T}{\partial n}+K_{ve}\frac{\partial T_{ve}}{\partial n}\right)+\left(\frac{\kappa}{1+n\kappa}+\frac{j\cos\theta}{r+n\cos\theta}\right)\times\left(K_{tr}\frac{\partial T}{\partial n}+K_{ve}\frac{\partial T_{ve}}{\partial n}\right)-\sum_{i=1}^{N_s}J_i^n\left(C_{p,tr}^i\frac{\partial T}{\partial n}+C_{p,ve}^i\frac{\partial T_{ve}}{\partial n}\right)+\mu\left(\frac{\partial u}{n}-\frac{u\kappa}{1+n\kappa}\right)^2\right]-\sum_{i=1}^{N_s}h_i\dot{w}_i \tag{1}$$

Vibrational–electronic–electron energy (temperature) equation:

$$\rho C_{p,ve}\left(\frac{u}{1+n\kappa}\frac{\partial T_{ve}}{\partial s}+v\frac{\partial T_{ve}}{\partial n}\right)=\sum_{i=\text{mol}}\rho_i\dot{w}_{v,i}+3\left(\frac{\gamma_\infty-1}{\gamma_\infty}\right)\rho_e(T-T_{ve})\sum_{\substack{i=1\\ i\neq e}}^{N_s}\left(\frac{\nu_{e,i}}{M_i}\right)-\sum_{i=\text{ions}}\dot{n}_{e,i}I_i+\sum_{i=\text{mol}}\dot{w}_i\hat{D}_i-\sum_{i=\text{mol}}h_{ve,i}\dot{w}_i+\frac{p_e}{\rho}\left(\frac{u}{1+n\kappa}\frac{\partial\rho}{\partial s}+\frac{\partial\rho}{\partial n}\right)+\varepsilon^2\left[\frac{\partial}{\partial n}\left(K_{ve}\frac{\partial T_{ve}}{\partial n}\right)+\left(\frac{\kappa}{1+n\kappa}+\frac{j\cos\theta}{r+n\cos\theta}\right)K_{ve}\frac{\partial T_{ve}}{\partial n}\right]-\varepsilon^2\sum_{i=1}^{N_s}J_i^nC_{p,ve}^i\frac{\partial T_{ve}}{\partial n} \tag{2}$$

Equation of state:

$$p=\sum_{\substack{i=1\\ i\neq e}}^{N_s}\rho_i\left(\frac{R^*}{M_i^*C_{p,\infty}^*}\right)T+p_e \tag{3a}$$

where

$$p_e=\rho_e\left(\frac{R^*}{M_e^*C_{p,\infty}^*}\right)T_{ve} \tag{3b}$$

In Eqs. (1) and (2), $j = 0$ for planar flow and $j = 1$ for axisymmetric flow are to be employed.

A translational–rotational energy equation may be obtained by subtracting Eq. (2) from Eq. (1). The resulting equation can also be used in place of Eq. (1) for obtaining the translational–rotational temperature T.

With vibrational and electronic nonequilibrium only (i.e., in the absence of ionization), air consists of five neutral species. For such a mixture, the total energy and vibrational energy equations are obtained from Eqs. (1) and (2) by deleting the underlined terms in Eq. (2).

Thermodynamic Properties

For the two-temperature model, the specific enthalpy for each species h_i is obtained from

$$h_i=(h_{tr,i}^*+h_{ve,i}^*)/U_\infty^{*2} \tag{4a}$$

where

$$h_{tr,i}^*=\int_{\bar{T}_{\text{ref}}^*}^{T^*}C_{p,tr}^{i*}\,dT^*+(\Delta h_i^{f*})_{\bar{T}_{\text{ref}}^*} \tag{4b}$$

$$h_{ve,i}^*=\int_{\bar{T}_{\text{ref}}^*}^{T_{ve}^*}C_{p,ve}^{i*}\,dT^*=e_{ve,i}^* \tag{4c}$$

In Eq. (4b), $C_{p,tr}^{i*}$ is $(7/2)R_i^*$ for diatomic species and $(5/2)R_i^*$ for monatomic species. The vibrational–electronic–electron portion of the specific heat $C_{p,ve}^{i*}$ in Eq. (4c) is calculated from[11]

$$C_{p,ve}^{i*}=C_p^{i*}(T_{ve}^*)-C_{p,tr}^{i*} \tag{5}$$

where $C_p^{i*}(T_{ve}^*)$ is evaluated from the curve fits[11,12] for C_p^{i*} using T_{ve}^*. The frozen mixture properties C_p and h are obtained from the individual species properties by employing the relations given in Ref. 12.

Transport Properties

The mixture viscosity μ is computed from[11]

$$\mu=\frac{1}{\mu_{\text{ref}}^*}\sum_{\substack{i=1\\ i\neq e}}^{N_s}\left\{\frac{M_i^*}{N_A^*}x_i\Big/\left[\sum_{\substack{j=1\\ j\neq e}}^{N_s}x_j\Delta_{ij}^{(2)*}(T^*)+x_e\Delta_{ie}^{(2)*}(T_{ve}^*)\right]\right\}+\frac{1}{\mu_{\text{ref}}^*}\frac{M_e^*}{N_A^*}x_e\Big/\left[\sum_{j=1}^{N_s}x_j\Delta_{ej}^{(2)*}(T_{ve}^*)\right] \tag{6}$$

where the modified collision integrals $\Delta_{ij}^{(1)*}$ and $\Delta_{ij}^{(2)*}$ are obtained from Ref. 11 in terms of the curve-fitted collision integrals $\pi\Omega_{ij}^{(1,1)*}$ and $\pi\Omega_{ij}^{(2,2)*}$, respectively.

The frozen thermal conductivity of the mixture for the translational and rotational energies of heavy particles K_{tr} is computed from the relation

$$K_{tr}=K_t+K_r \tag{7}$$

where the translational K_t and rotational K_r components are given in Refs. 11 and 12.

The frozen thermal conductivity of the mixture for the vibrational and electronic excitation energies and free electrons K_{ve} is obtained from the following expression:

$$K_{ve}=K_v+K_{\text{el}}+K_e \tag{8}$$

where the vibrational K_v, electronic K_{el}, and electron components may be obtained from Ref. 11 or 12.

The diffusion mass flux of species i, J_i^n is computed with the assumption that the remainder of the species in the mixture move with the same velocity or are stationary. For such calculations, an effective diffusion coefficient D_{im} can be defined as[3,15]

$$D_{im}=(1-x_i)\Big/\sum_{\substack{j=1\\ j\neq i}}^{N_s}(x_j/D_{ij}) \tag{9a}$$

where

$$D_{ij} = (9.8692 \times 10^{-7}) \left(\frac{k^*}{\mu^*_{\text{ref}} C^*_{p,\infty}}\right) \frac{T}{p\Delta^{(1)}_{ij}{}^*(T^*)} \tag{9b}$$

for diffusion between heavy particles and

$$D_{ej} = (9.8692 \times 10^{-7}) \left(\frac{K^*}{\mu^*_{\text{ref}} C^*_{p,\infty}}\right) \frac{T_{ve}}{p\Delta^{(1)}_{ej}{}^*(T^*_{ve})} \tag{9c}$$

for diffusion between electrons and heavy particles.

For ions, the ambipolar diffusion coefficient D^a_{im} (which has double the value of ionic diffusion coefficient) is introduced because of ambipolar diffusion approximation, i.e.,

$$D^a_{im} = 2D_{im} \qquad (i = \text{ions}) \tag{9d}$$

The effective diffusion coefficient for electrons is computed using

$$D_{em} = m^*_e \sum_{i=\text{ions}} D^a_{im} x_i \Bigg/ \left(\sum_{i=\text{ions}} \frac{M^*_i}{N_A} x_i\right) \tag{9e}$$

where m^*_e is the mass of an electron, and N_A is Avogadro's number.

Chemical Kinetics Model and Chemical–Vibrational Coupling

The chemical reactions with the appropriate rate-controlling temperature for the forward- and backward-rate coefficients are given in Table 1 of Ref. 12. The forward and backward electron–impact ionization reactions and backward associative ionization reactions are controlled by T_{ve}. Other reactions are governed only by the translational temperature. The backward-rate coefficients given in Table 1 of Ref. 12 are used for temperatures to 14,000 K (temperature range of their validity[11]). For temperatures greater than 14,000 K, the backward-rate coefficients are evaluated by using

$$k^*_{b,r} = k^*_{f,r}(T^*)/K_{\text{eq},r}(T^*) \tag{10}$$

where $K_{\text{eq},r}$ are the equilibrium constants obtained using the atomic and molecular partition functions and are computed from the curve fits of Ref. 11. To ensure a smooth transition from low-to-high temperature range, the backward-rate coefficients obtained from Table 1 and Eq. (10) are linearly averaged over an overlap region of 4000 K between 10,000–14,000 K.

In general, an 11-species (N_2, O_2, N, O, NO, NO^+, N^+, O^+, N_2^+, O_2^+, and e^-) air model (with reactions 1–20 in Table 1 of Ref. 12) is employed. However, for vibrational and electronic nonequilibrium only, a five-species (N_2, O_2, N, O, and NO) air model (with reactions 1 through 6), or for weakly ionized flows, a seven-species (N_2, O_2, N, O, NO, NO^+, and e^-) air model (with reactions 1–7 in Table 1 of Ref. 12) can be used. To consider the effect of chemical–vibrational coupling, Park's model[12,16] for preferential dissociation and recombination is used. In Park's two-temperature model,[16] it is assumed that the forward dissociation reactions are characterized by the rate-controlling temperature T^*_a:

$$T^*_a = T^{*1-q} T^{*q}_{ve} \tag{11a}$$

where the exponent q is defined (following the suggestion of Hansen[17]) as

$$q = 0.1 + 0.4(T^*_{ve}/T^*) \tag{11b}$$

The way the production terms $(\dot{w}_i/\rho)$ are treated is very important to overcome the stiffness problems encountered near chemical and thermal equilibrium conditions. The chemical stiffness problem is addressed by following the approach of Ref. 18. To overcome the thermal stiffness problem in the energy equations, the production term $(\dot{w}_i/\rho)$ is expanded in a series as

$$(\dot{w}_i/\rho)^{k+1} = (\dot{w}_i/\rho)^k + \left[\frac{\partial}{\partial T}(\dot{w}_i/\rho)\right]^k_{p,T_{ve},C_i} \times (T^{k+1} - T^k) \tag{12a}$$

where k denotes iteration number for which the solution is known and

$$\left(\frac{\partial \rho}{\partial T}\right)_{p,T_{ve},C_i} = -\left(1 - \frac{p_e}{p}\right)\frac{\rho}{T} \tag{12b}$$

The term $\Sigma_{i=1}^{N_s} h_i \dot{w}_i$, which appears in Eq. (1), is written as[18]

$$\sum_{i=1}^{N_s} h_i \dot{w}_i = \dot{w}_1 + \dot{w}_2 T \tag{13}$$

and the term $\Sigma_{i=\text{mol}} h_{ve,i}\dot{w}_i$, which appears in Eq. (2), is written as

$$\sum_{i=\text{mol}} h_{ve,i}\dot{w}_i = \sum_{i=\text{mol}} h_{ve1,i}\dot{w}_i + T_{ve} \sum_{i=\text{mol}} \tilde{h}_{ve2,i}\dot{w}_i \tag{14a}$$

where $h_{ve1,i}$ and $\tilde{h}_{ve2,i}$ are related to $h_{ve,i}$ as follows:

$$(h_{ve,i})^{k+1} = (h_{ve,i})^k + \left(\frac{\partial h_{ve,i}}{\partial T_{ve}}\right)^k (T^{k+1}_{ve} - T^k_{ve}) \tag{14b}$$

$$= [(h_{ve,i})^k - C^k_{v,ve,i} T^k_{ve}] + (C^k_{v,ve,i} T^{k+1}_{ve}) \tag{14c}$$

$$= h^k_{ve1,i} + (\tilde{h}_{ve2,i})^k T^{k+1}_{ve} \tag{14d}$$

and k is the iteration number.

Vibrational Energy Reactive Source Term

The term $\Sigma_{i=\text{mol}} \dot{w}_j \hat{D}_i$ represents the vibrational energy lost/gained because of dissociation/recombination of molecules. The value of $\hat{D}_i$ is generally taken as a fraction of the dissociation energy $\tilde{D}_i$ of a molecule. Thus,

$$\hat{D}_i = \hat{c}_1 \tilde{D}_i \tag{15}$$

where $0 < \hat{c}_1 < 0.5$ and $\tilde{D}_i$ is given in Table 1 of Ref. 3. The vibrational energy equations used in earlier work [Eq. (5) of Ref. 9 and Eq. (78) of Ref. 19], did not contain this term. However, recent work of Lee[20] included this term.

Electronic Energy Reactive Source Term

The electronic energy reactive source term $\Sigma_{i=\text{ions}} \dot{n}_{e,i} I_i$ accounts for the electron energy loss because of electron-impact ionization. Here, $\dot{n}_{e,i}$ is the net rate of such ionization (producing O^+ and N^+ in reactions (17) and (18) for an 11-species air model given in Table 1 of Ref. 12), and I_i is the first ionization energy of the species (provided in Table 1 of Ref. 3).

Translational–Vibrational Energy Exchange (Relaxation) Term

The expression for the translational–vibrational energy exchange term $\Sigma_{i=\text{mol}} \rho_i \dot{w}_{v,i}$ is[13,16]

$$\sum_{i=\text{mol}} \rho_i \dot{w}_{v,i} = \rho \sum_{i=\text{mol}} C_i \left[\frac{C^i_{v,ve}(T - T_{ve})}{\tau_i}\right] \times \left|\frac{T - T_{ve}}{T_{\text{sh}} - T_{ve,\text{sh}}}\right|^{s-1} \tag{16a}$$

where

$$s = 3.5 \exp(5000/T^*_{\text{sh}}) \tag{16b}$$

The relaxation time of species i, τ_i, in Eq. (16a) is given as combination of the Landau–Teller type relaxation time ($\langle\tau_i\rangle$) and the collision limited relaxation time τ_{ci}, such that[13]

$$\tau_i = \langle\tau_i\rangle + \tau_{ci} \tag{17}$$

where the definitions of $\langle\tau_i\rangle$ and τ_{ci} used in this work are provided in Ref. 12.

The definition of τ_{ci} in Ref. 12 contains total number density n^* in place of the species number density used in Eq. (56) of Ref. 3. This change corrects an error in this reference. Also, the limiting collision cross section σ_v^* is assumed to be[16]

$$\sigma_v^* = 10^{-17}(50{,}000/T^*)^2 \tag{18}$$

Translational–Electron Energy Exchange (Relaxation) Term

This term

$$3\left(\frac{\gamma_\infty - 1}{\gamma_\infty}\right)\rho_e(T - T_{ve})\sum_{\substack{i=1\\ i\neq e}}^{N_s}\left(\frac{\nu_{e,i}}{M_i}\right) \tag{19a}$$

with

$$\nu_{e,i} = \nu_{e,i}^*/(U_\infty^*/R_N^*) \quad \text{and} \quad M_i = (M_i^*/\bar{M}_\infty^*) \tag{19b}$$

represents the energy transfer rate between the heavy particle and electron translational modes. The expressions for the effective collision frequency for collisions between electrons and neutrals and for Coulomb collisions between electrons and ions are given in Ref. 3, and the same are used here.

Boundary Conditions

The body-slip boundary conditions used in this study are those of Ref. 21. These boundary conditions for tangential velocity u_s, pressure p_s, translational–rotational temperature T_s, and species concentrations C_i^s with higher-order slip effects are provided in Ref. 12.

The body-slip value of the vibrational–electronic–electron temperature is assumed to be equal to the translational–rotational temperature value, i.e.,

$$T_{ve,s} = T_s \tag{20}$$

The translational–rotational slip temperature with a radiative equilibrium wall assumption is computed from

$$(T_s)_{\text{REWT}} = \frac{1}{T_{\text{ref}}^*}\left\{-\frac{\varepsilon^2}{\sigma^*\bar{\varepsilon}}\rho_\infty^* U_\infty^{*3}\left[K_{tr}\frac{\partial T}{\partial n} + K_{ve} \times \frac{\partial T_{ve}}{\partial n} - \sum_{i=1}^{N_s} h_i J_i^n\right]_s\right\}^{1/4} \tag{21}$$

where REWT is the radiative equilibrium wall temperature).

Boundary conditions for a noncatalytic and a fully catalytic wall are specified by Eqs. (22) and (23), respectively,

$$\left(\frac{\partial C_i}{\partial n}\right)_s = 0 \tag{22}$$

$$C_i^s = [C_i(p_s, T_s)]_{\text{eq}} \tag{23a}$$

i.e., the mass fractions are calculated to be the equilibrium (thermal and chemical) values at the slip temperature and pressure. For the case of no injection and a highly cooled surface, Eq. (23a) simplifies to

$$C_i^s = C_{i,\infty} \tag{23b}$$

The shock-slip boundary conditions employed for variables v_{sh}, u_{sh}, p_{sh}, and $C_{i,\text{sh}}$ for a two-temperature model are similar to those given in Refs. 22 and 23 for one-temperature (thermal equilibrium) formulation. The boundary conditions used for the two energy equations are obtained in Ref. 12.

No-slip boundary conditions at the body and shock are obtained in the limit of ε approaching zero, and by replacing the subscript and superscript s by w in the slip conditions given here and in Ref. 12. With zero slip ($\varepsilon = 0$), Eq. (33) of Ref. 12 gives the usual frozen-flow approximation, which assumes the flow to be frozen at the freestream composition behind the shock. Also, simplification of Eq. (35a) in Ref. 12 for no-slip condition gives $T_{ve,\text{sh}} = T_\infty$, which implies that the vibrational–electronic–electron temperature behind the shock is equal to the freestream temperature.

The boundary conditions given in Ref. 12 are valid for a one-temperature (thermal equilibrium) model also with the assumption of $T_{ve} = T$.

Method of Solution

The overall method for the solution of VSL equations with thermochemical nonequilibrium and slip conditions is similar to that described in Refs. 23–25. This method is a spatial-marching, implicit, finite difference technique, which includes coupling of the global continuity and normal momentum equations. The solution with thermal and chemical nonequilibrium, and body and shock slip at a given body station m is determined in the following manner:

1) Make an initial guess for all shock and profile quantities.

2) Compute slip quantities at shock and body.

3) Solve species concentration equations for C_i first, and then solve the vibrational–electronic–electron energy equation for T_{ve}, total energy equation for translational–rotational temperature T, and equation of state for ρ in this sequence.

4) Compute thermodynamic and transport properties using T and T_{ve}.

5) Solve the s-momentum equation for u, continuity equation for n_{sh}, continuity and n-momentum equations simultaneously for v and p, and equation of state for ρ.

6) Repeat steps 1–5 until convergence is obtained for all of the flowfield variables at each point of the finite difference grid. A flow-chart for the solution sequence outlined here is given in Ref. 12. The converged solution at body station m is used as an initial guess to march the solution downstream for a global (streamwise) sweep. Typically, three or four global sweeps are needed to obtain a converged shock shape (and a globally converged solution).

A normal grid with 101 points is clustered both at the body surface and shock to capture large gradients in the nonequilibrium flow properties there. The minimum grid spacing Δn in the normal direction is of the order of 10^{-4} for obtaining a grid-independent solution with the variable ε value of 0.01. The grid is changed in inverse proportion to the density for a different altitude condition. In the streamwise direction, a grid spacing Δs of 0.1 is used generally. The CPU time required is 0.009 s/grid-point/iteration on Cray Y-MP8E machine at the NASA Langley computer center for an 11-species flowfield calculation with thermochemical nonequilibrium. With thermal equilibrium, this value decreases by about 20%, whereas with the inclusion of surface and shock-slip, this value increases by about 30%. The computer memory requirement is about 380 kilowords with 64-bit precision. These computer resource (CPU time for converged solutions and memory) requirements are about an order of magnitude smaller than those for the Navier–Stokes Langley aerothermodynamic upwind relaxation algorithm (LAURA) calculations[3] for an axisymmetric body at 0-deg angle of attack.

Results and Discussion

Numerical results, obtained from the solution of the viscous shock-layer equations for air in thermochemical nonequilib-

rium, are discussed in this section. Results presented here include comparisons with some of the flight experiments and existing calculations for re-entry flows under thermal nonequilibrium conditions. For thermal equilibrium conditions, the parent VSL code has been compared extensively with the flight and wind-tunnel data.[14,24,25] Results are also obtained for the nose region of a proposed SSTO vehicle[2] along an assumed entry trajectory. First, a brief discussion of the modeling of vibrational energy source term and its influence on numerical predictions is provided.

Energy Exchange in Dissociation and Its Effect on Flowfield Calculations

As mentioned earlier, the vibrational energy source term $\Sigma_{i=\text{mol}}\, \dot{w}_i \hat{D}_i$ (with $\hat{D}_i = \hat{c}_1 \hat{D}_i$) in Eq. (2) represents the vibrational energy lost or gained because of molecular dissociation or recombination. References 3 and 20 have modeled this term with $0 < \hat{c}_1 \leq 1$. A large value of $\hat{c}_1$ (=0.8) tends to substantially lower the vibrational temperature behind the shock where dissociation occurs, and substantially raises the vibrational temperature in the boundary layer where recombination occurs.[3] On the other hand, employing $\hat{c}_1 = 0$ results in the persistence of considerable thermal nonequilibrium in the cooler, high-density regions closer to a body surface (see Fig. 6 of Ref. 12). For the case considered in that figure with radiative equilibrium wall temperature, a value of $\hat{c}_1 = 0.25$ gives translational and vibrational temperatures that are consistent with the thermally equilibrated value as shown in Fig. 1 of this article. The translational and vibrational temperature profiles of this figure are qualitatively similar to those of Fig. 7 in Ref. 9. The differences between the two results are because of different values of $\hat{c}_1$ used and differences in the chemistry models (Ref. 11 vs Ref. 16 of Ref. 9) employed. Further, the effect of vibrational temperature on reaction rate constants is not accounted for in Refs. 9 and 10. Stagnation-point values of the presently computed wall heat flux are 158.4 and 156.2 W/cm^2 for thermal equilibrium and nonequilibrium cases with radiative equilibrium surface temperatures of 1322 and 1318 K, respectively. These are approximately the same as those shown in Fig. 5 of Ref. 26. Clearly, the effect of thermal nonequilibrium (shown in Fig. 7 of Ref. 12) is negligible on convective heating for this case.

Comparison with RAM-C Flight Experiment

The first comparison of the predicted values with the flight data is made with those obtained from the RAM-C II vehicle. This was one of the three radio attenuation measurement test vehicles[27–29] for the investigation of flowfield plasma near reentry velocity (~7.6 km/s) conditions. The vehicle was a 9-deg spherically blunted cone with a nose radius of 0.1524 m and had a total length of 1.295 m. It was instrumented to measure electron number density across the shock layer. Microwave reflectometers were used to measure the peak values of electron number densities at four axial locations, whereas a langmuir probe rake (extending across the shock layer at the base of the cone) measured electron number density profiles. Calculations have been performed at three altitudes of 61, 71, and 80.8 km to compare with the data. Freestream conditions for these altitudes are tabulated in Ref. 12. The vehicle surface is assumed to be fully catalytic at a fixed temperature of 1000 K, whereas the calculations of Candler and MacCormack[5] employed a noncatalytic wall boundary condition at a constant temperature of 1500 K. Their boundary condition moves the peak number density prediction close to the wall.[30] Present calculations employ an 11-species chemical model for air. Experimental data and computed values for peak electron number density along the axis of the RAM-C II vehicle are shown in Fig. 2. Presently computed and the LAURA values[30] (at 71 km altitude) compare quite well with data. Comparison of the predicted electron number density profiles across the shock layer with experimental values is shown in Fig. 3. Present predictions are in good agreement with data, whereas the LAURA values[30] are somewhat higher near the surface at 80.8 km altitude. Present calculations include body and shock-slip boundary conditions and, similar to LAURA, are based on a two-temperature (2-T) formulation. One-temperature (1-T) and zero body- and shock-slip calculations of Dunn and Kang[31] give higher values at 80.8 km altitude and lower values at 71 km altitude as compared to the data. Clearly, the present predictions with slip boundary conditions and thermal nonequilibrium flowfield model are in better agreement with data as compared to the calculations of Refs. 30 and 31. There are slight differences in the chemical kinetic models used and the values of the energy loss fraction $\hat{c}_1$ employed here and in Ref. 30. A value of $\hat{c}_1 = 0.25$ is used in Eq. (12), whereas Ref. 30 has employed $\hat{D}_1 = h_{ve,i}$ in place of Eq. (12). The effect of employing different values of $\hat{c}_1$ on energy exchange in dissociation is discussed earlier. Comparisons of Figs. 2 and 3 show that the accuracy of the electron density predictions obtained from the present two-temperature formulation with body and shock-slip boundary conditions are quite good.

Comparison with FIRE II Flight Data

The FIRE II vehicle was instrumented[32] to measure total heating rates (convective plus absorbed radiative), radiative intensity in the 0.2–6.2 eV range, and spectral radiation in the 2–4 eV interval. Only the stagnation-point measurements are used for comparison with the present predictions. The fore-

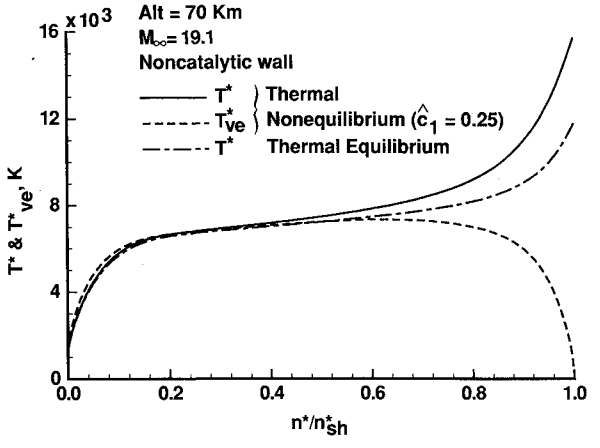

Fig. 1 Stagnation-point temperature profiles with and without thermal equilibrium.

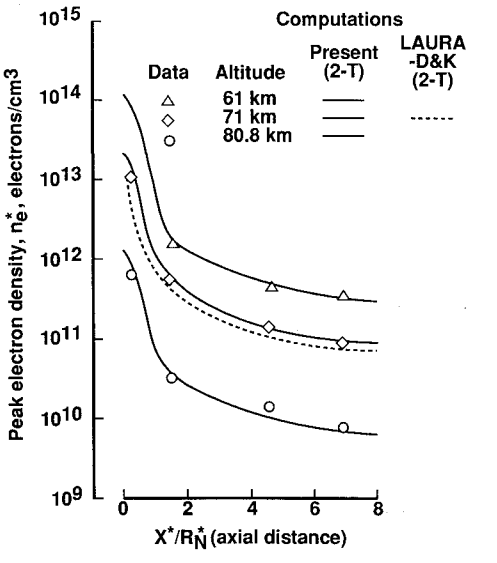

Fig. 2 Comparison of predicted peak electron density with experimental data for RAM-C II vehicle.

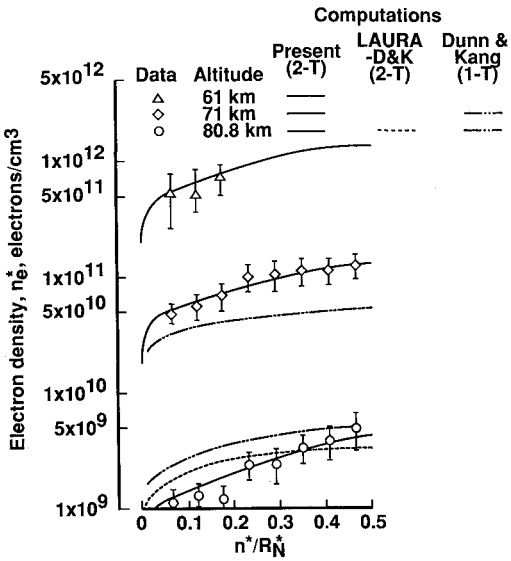

Fig. 3 Predicted and experimental profiles of electron density across the shock layer of RAM-C II vehicle.

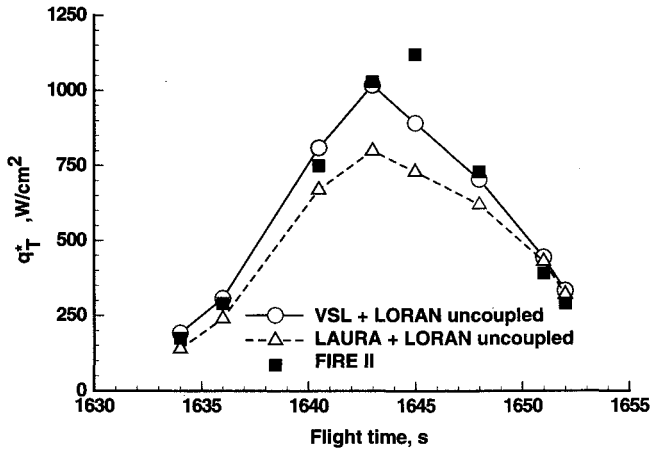

Fig. 4 Comparison of predicted stagnation-point total wall heat flux with data from FIRE II.

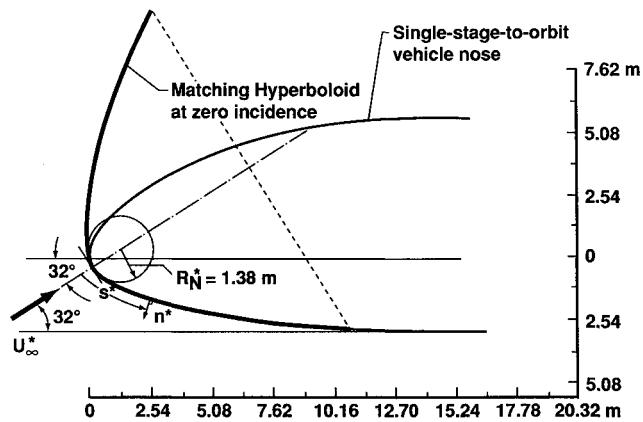

Fig. 5 Coordinate system of the matching hyperboloid for nose region of a proposed SSTO vehicle at 32-deg angle of attack.

body configuration for the FIRE II vehicle was a truncated hemispherical shape with a small corner radius. The vehicle heat shield consisted of three beryllium layers. For the present study, equivalent hemispherical nose radii[33,34] of 0.747, 0.656, and 0.600 m were used for the three heat shield layers. The freestream conditions are tabulated in Refs. 12 and 33. A comparison of the computed total heat flux with FIRE II data[32] is shown in Fig. 4. The VSL + Langley optimized radiative nonequilibrium (LORAN) uncoupled values are from Table 5 of Ref. 12. In this table, the VSL convective heating results have been obtained by the present method, whereas the uncoupled LORAN radiative heating values are taken from Ref. 7. LORAN is a nonequilibrium radiative heating prediction method[35] and treats the radiation spectrum in moderate detail, accounting for all mechanisms of importance. The LAURA convective heating values are also obtained in Ref. 7. Except for the flight time of 1645 s, there is a very good agreement of the presently predicted VSL results + LORAN values (of Ref. 7) with data, especially for the earlier flight times when thermal nonequilibrium is more significant. The LAURA + LORAN uncoupled results are consistently lower than the flight and VSL + LORAN values, except for later flight times (1651 s and beyond). At the peak computational heating point (1643 s), the LAURA + LORAN values are lower by about 20% as compared to the flight data and VSL + LORAN values. As mentioned earlier, the differences in the VSL and LAURA convective heating rates are because of the differences in physical models employed. The two methods use different chemical kinetics models, values for $\hat{c}_1$, degrees of vibrational and electronic excitations (i.e., partial or full) in the thermal conductivity calculations, and curve-fits for the collision integrals for transport properties. Since VSL is a rapid calculation procedure, present VSL results contain more detailed flowfield physics (without significantly increasing the computational time) as compared to the LAURA results of Ref. 7.

Stagnation-Region Flowfield Analysis and Heating Rates for a SSTO Vehicle Trajectory

A detailed flowfield analysis of the stagnation region of a proposed SSTO vehicle[2] has been carried out with the two-temperature viscous shock-layer technique presented here. The flowfield structure and surface heating rates along the SSTO vehicle windward centerline plane have been obtained by seeking solutions over the matching hyperboloid at zero incidence (see Fig. 5). This modeling is possible only for the nose region because, unlike the Shuttle,[36] the SSTO vehicle (whose nose region is shown in Fig. 5) does not have a flat bottom surface. However, the windward-side surface in the windward centerline plane does have a smoothly decreasing slope, which essentially becomes constant over the aft portion of the vehicle. The half-angle θ of the equivalent hyperboloid employed is 32 deg, with an R_N^* of 1.38 m. Calculations have been performed at four points in the trajectory near the peak heating point (at 65 km altitude) using the freestream conditions given in Table 1. The catalytic recombination coefficient $\bar{\gamma}_i$ values used for the vehicle surface (assumed to be similar to that of a shuttle) are

$$\bar{\gamma}_N = 0.007 \exp(-2219/T_w^*), \quad 950 \text{ K} < T_w^* < 1670 \text{ K} \quad (24a)$$

$$\bar{\gamma}_0 = 8 \exp(-8600/T_w^*), \quad 1000 \text{ K} < T_w^* < 1650 \text{ K} \quad (24b)$$

and the surface is considered to be at radiative equilibrium wall temperature (T_{REWT}^*). Equation (24) for the surface recombination coefficients has been established from flight heat-flux measurements (obtained from the early Shuttle flight test missions), by employing a procedure similar to that of Ref. 37. Equation (24), however, has been obtained after making corrections, changes, and a grid resolution study with a recently developed partially coupled viscous shock-layer code.[25]

The first set of calculations is done at 65 km altitude to evaluate the effect of the model used for the vibrational energy reactive source term. Similar to the results given in Fig. 7 of Ref. 12, a value of $\hat{c}_i = 0.25$ in the vibrational energy source term gives translational and vibrational temperatures consistent with the thermally equilibrated value as shown in Fig. 6.

Selected stagnation-point results at four altitudes for the freestream conditions given in Table 1 are provided in Table 2. The tabulated values include shock and surface quantities

Table 2 Selected stagnation-point results for a proposed SSTO vehicle

Altitude, km	p^*_{sh}, atm				T^*_{sh}, K				$\rho^*_{sh}/\rho^*_\infty$			
	No slip		Body and shock-slip		No slip		Body and shock-slip		No slip		Body and shock-slip	
	TE	TNE	TE	TNE	TE	TNE	TE	TNE	TE	TNE	TE	TNE
85	4.491×10^{-3}	4.146×10^{-3}	4.525×10^{-3}	4.164×10^{-3}	19,078	29,896	14,874	25,179	10.086	5.943	10.836	6.066
75	1.775×10^{-2}	1.649×10^{-2}	[b]	[b]	16,472	24,499	[b]	[b]	9.491	5.931	[b]	[b]
65[a]	4.645×10^{-2}	4.379×10^{-2}	[b]	[b]	11,867	15,928	[b]	[b]	8.392	5.895	[b]	[b]
55	7.086×10^{-2}	6.764×10^{-2}	[b]	[b]	5,872	7,264	[b]	[b]	7.479	5.771	[b]	[b]
	p^*_w, atm				T^*_{REWT}, K				q^*_w, W/cm^2			
85	4.797×10^{-3}	4.732×10^{-3}	4.017×10^{-3}	4.130×10^{-3}	1,394	1,314	1,368	1,300	19.352	15.263	17.933	14.637
75	1.908×10^{-2}	1.898×10^{-2}	[b]	[b]	1,604	1,584	[b]	[b]	33.976	32.256	[b]	[b]
65[a]	5.043×10^{-2}	5.031×10^{-2}	[b]	[b]	1,609	1,606	[b]	[b]	34.383	34.062	[b]	[b]
55	7.725×10^{-2}	7.704×10^{-2}	[b]	[b]	1,310	1,309	[b]	[b]	15.108	15.055	[b]	[b]

[a]Peak heating altitude. [b]Slip effects negligible.

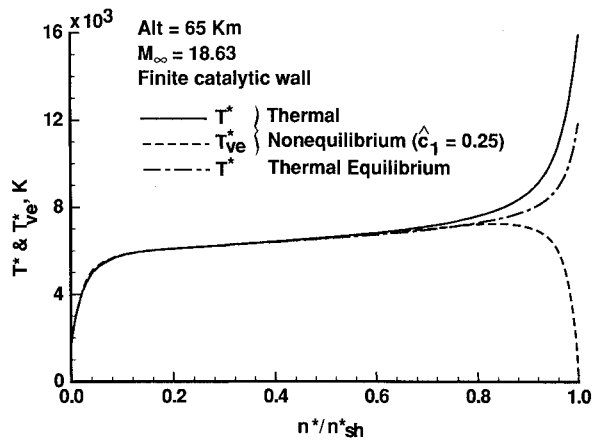

Fig. 6 Stagnation-point temperature profiles for thermal equilibrium and nonequilibrium conditions (with $c_1 = 0.25$).

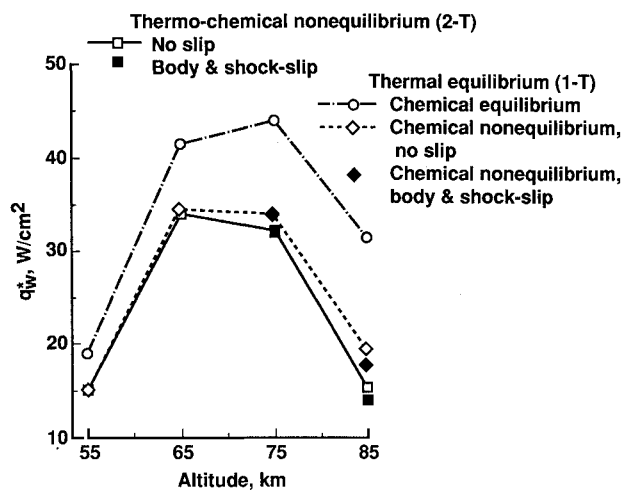

Fig. 7 Thermochemical nonequilibrium and equilibrium stagnation heating for a proposed SSTO vehicle.

with thermal equilibrium and nonequilibrium and without slip for altitudes of 55, 65, 75, and 85 km. For 85 km altitude, various values with body and shock-slip are also obtained. At 75 km altitude, the effects of body and shock-slip on various quantities are negligible and, therefore, the lower altitude cases were not run with the slip boundary conditions. Further, except for the altitude of 85 km, the effect of thermal nonequilibrium is more noticeable on shock than wall quantities and decreases with decreasing altitude. At an altitude of 85 km, the effect of thermal nonequilibrium is to lower the wall heat flux by about 21% without slip and 23% with slip effects as compared to

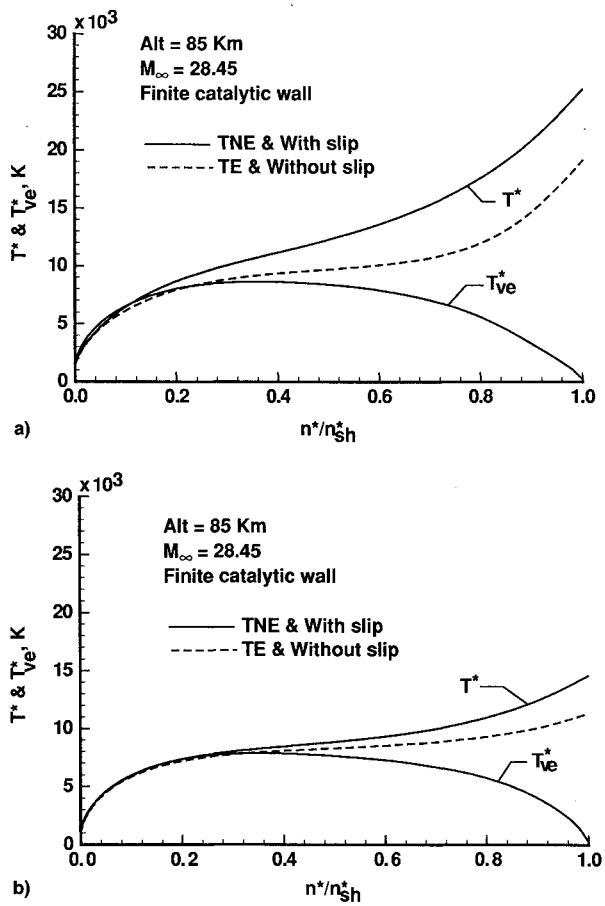

Fig. 8 Effect of slip and TNE on temperature profiles. s = a) 0.0 and b) 2.0.

the respective thermal equilibrium values. The effect of slip is to decrease the wall heat flux by about 7% with thermal equilibrium and 4% with thermal nonequilibrium relative to the corresponding no-slip values. Obviously, at 85 km altitude, thermal nonequilibrium effects are more important than the slip effects for wall heat flux calculations. The combined effects of thermal nonequilibrium and slip conditions lowers the heating by about 24% as compared to the no-slip thermal equilibrium value at this altitude. Some observations from the design standpoint can be made regarding the thermal protection system (TPS) for the nose-cap, based on the surface temperatures provided in Table 2. The stagnation-point radiative equilibrium wall temperature exceeds 1600 K at the peak-heating altitude of 65 km. Temperatures greater than 1600 K are outside[38] the multiuse limits of ceramic TPS with reaction-cured

glass (RCG) coatings [characterized by recombination coefficient values of Eqs. (24a) and (24b)], but within the limits of reinforced carbon–carbon (RCC)/advanced carbon–carbon (ACC), which are materials typically used in the construction of a vehicle nose-cap thermal protection system.

Figure 7 summarizes the surface heating results of Table 2. Also included in this figure are the thermochemical equilibrium (one-temperature) results obtained by the method of Ref. 39. These values are generally considered as upper limits of surface heat flux for heat shield design purposes. As can be seen from this figure, chemical nonequilibrium persists even at an altitude of 55 km. For this altitude, the nonequilibrium heating (for a Shuttle-like surface) is about 21% lower than the chemical equilibrium value.

The temperature profiles at the stagnation point ($s = 0$) and two nose radii ($s = 2.0$) downstream, with and without body- and shock-slip and thermal nonequilibrium, are presented in Figs. 8a and 8b. In general, the slip and thermal nonequilibrium effects are maximum at the stagnation point (see Fig. 8a), and diminish downstream as shown in Fig. 8b. Detailed species profiles at the stagnation point and downstream are given in Ref. 12. The effect of slip and thermal nonequilibrium on species profiles is similar to that observed in the temperature profiles. Further, with thermal nonequilibrium, a higher level of dissociation and ionization is seen because of the larger weighting of the translational temperature [which is higher than the thermally equilibrated value], in the dissociation temperature equation [Eq. (11)].

Conclusions

A two-temperature VSL technique is presented for analyzing an 11-species airflow with thermochemical nonequilibrium. The present formulation employs recently developed physical models, detailed transport and thermodynamic properties, and body and shock-slip boundary conditions (required for the low-density flows associated with thermal nonequilibrium) for multicomponent mixtures.

Results obtained with the present method reproduce examined re-entry flight data with a good degree of accuracy over a wide range of conditions, validating its use for the calculation of low-to-high density flows. These results also agree fairly well with the existing calculations.

Detailed stagnation-region flowfield calculations have been carried out at four altitudes of 55, 65, 75, and 85 km along the trajectory of a proposed SSTO vehicle. Of these four altitudes considered, thermal nonequilibrium (with significant vibrational and electronic nonequilibrium components) and slip effects are important only at 85 km altitude, where the stagnation-point heating is about 40% of the peak-heating value of ~34 W/cm^2 at 65 km altitude. The combined effects of thermal nonequilibrium and slip conditions lower the heating by about 24%. The effect of slip is negligible for altitudes lower than 75 km, whereas the effect of thermal nonequilibrium on surface quantities becomes negligible at 55 km altitude. At this altitude, however, the chemical nonequilibrium effects lower the stagnation heating obtained from chemical equilibrium calculations by about 21% for the Shuttle-like surface. These results demonstrate the use of VSL technique as a quick method with minimum computer resource (memory and computational time) requirements to evaluate slip effects and vibrational and electronic nonequilibrium along the trajectory of a flight vehicle. This capability is very desirable in a conceptual or preliminary design process, requiring analysis of many trajectory points.

Acknowledgments

The author would like to thank K. P. Lee for the help in obtaining some of the results reported here and J. N. Moss, R. A. Mitcheltree, and P. A. Gnoffo for many helpful suggestions during preparation of the manuscript.

References

[1]Austin, R. E., and Cook, S. A., "SSTO Rockets: Streamlining Access to Space," *Aerospace America*, Vol. 32, Nov. 1994, pp. 34–39.

[2]Weilmuenster, K. J., Gnoffo, P. A., Greene, F. A., Riley, C. J., Hamilton, H. H., II, and Alter, S. J., "Hypersonic Aerodynamic Characteristics of a Proposed Single-Stage-to-Orbit Vehicle," AIAA Paper 95-1850, June 1995.

[3]Gnoffo, P. A., Gupta, R. N., and Shinn, J. L., "Conservation Equations and Physical Models for Hypersonic Air Flows in Thermal and Chemical Nonequilibrium," NASA TP 2867, Feb. 1989.

[4]Palmer, G., "The Development of an Explicit Thermochemical Nonequilibrium Algorithm and Its Application to Compute Three Dimensional AFE Flowfields," AIAA Paper 89-1701, June 1989.

[5]Candler, G. V., and MacCormack, R. W., "Computation of Weakly Ionized Hypersonic Flow in Thermo-Chemical Nonequilibrium," *Journal of Thermophysics and Heat Transfer*, Vol. 5, No. 3, 1991, pp. 266–273.

[6]Walters, R. W., Cinnella, P., Slack, D. C., and Holt, D., "Characteristic-Based Algorithms for Flows in Thermochemical Nonequilibrium," *AIAA Journal*, Vol. 30, No. 5, 1992, pp. 1304–1313.

[7]Greendyke, R. B., and Hartung, L. C., "A Convective and Radiative Heat Transfer Analysis for the Fire II Forebody," AIAA Paper 93-3194, July 1993.

[8]Gally, T. A., and Carlson, L. A., "Survey of Nonequilibrium Re-Entry Heating for Entry Flight Conditions," AIAA Paper 93-3230, July 1993.

[9]Nishida, M., and Sakamura, Y., "Thermal and Chemical Nonequilibrium Viscous Shock Layer Flows over a Blunt Body at High Altitudes," *Rarefied Gas Dynamics*, edited by A. E. Beylich, *Proceedings of the 17th International Symposium on Rarefied Gas Dynamics Aachen 1990*, VCH Publishers, New York, 1991, pp. 514–521.

[10]Suzuki, K., and Abe, T., "Viscous Shock-Layer Analysis of Thermally and Chemically Non-Equilibrium Forebody Flow of Mars Aerocapture Vehicle," AIAA Paper 93-2839, July 1993.

[11]Gupta, R. N., Yos, J. M., Thompson, R. A., and Lee, K.-P., "A Review of Reaction Rates and Thermodynamic and Transport Properties for an 11-Species Air Model for Chemical and Thermal Nonequilibrium Calculations to 30,000 K," NASA RP 1232, Aug. 1990.

[12]Gupta, R. N., and Lee, K. P., "Thermo-Chemical Nonequilibrium Analysis of Viscous Shock-Layers," AIAA Paper 95-2083, June 1995.

[13]Park, C., *Nonequilibrium Aerothermodynamics*, Wiley, New York, 1990, pp. 103–115.

[14]Gupta, R. N., Lee, K.-P., and Zoby, E. V., "Enhancements to Viscous-Shock-Layer Technique," *Journal of Spacecraft and Rockets*, Vol. 30, No. 4, 1993, pp. 404–413.

[15]Bird, R. B., Stewart, W. E., and Lightfoot, E. N., *Transport Phenomena*, Wiley, New York, 1960, pp. 563–572.

[16]Park, C., "Assessment of Two-Temperature Kinetic Model for Ionizing Air," AIAA Paper 87-1574, June 1987.

[17]Hansen, C. F., "Collision-Induced Gas Phase Dissociation Rates," Final Rept. on NASA Grant NAG1-1046, Aug. 1990.

[18]Blottner, F. G., "Finite-Difference Methods of Solution of the Boundary-Layer Equations," *AIAA Journal*, Vol. 8, No. 2, 1970, pp. 193–206.

[19]Lee, J. H., "Basic Governing Equations for the Flight Regimes of Aeroassisted Orbital Transfer Vehicles," edited by H. F. Nelson, Vol. 96, Progress in Aeronautics and Astronautics, AIAA, New York, 1985, pp. 3–53.

[20]Lee, J. H., "Hypersonic Three-Dimensional Nonequilibrium Boundary-Layer Equations in Generalized Curvilinear Coordinates," NASA CR-185677, Feb. 1993.

[21]Gupta, R. N., Scott, C. D., and Moss, J. N., "Slip-Boundary Equations for Multicomponent Nonequilibrium Airflow," NASA TP-2452, Nov. 1985.

[22]Gupta, R. N., and Nayani, S. N., "Low-Density Flow Effects for Hyper-Velocity Vehicles," Air Force Flight Dynamics Lab., WRDC-TR-90-3007, Wright–Patterson AFB, OH, March 1990.

[23]Gupta, R. N., Nayani, S. N., Lee, K. P., and Zoby, E. V., "Higher-Order Viscous Shock-Layer Solutions for High-Altitude Flows," *Journal of Spacecraft and Rockets*, Vol. 31, No. 5, 1994, pp. 751–758.

[24]Lee, K. P., Gupta, R. N., Zoby, E. V., and Moss, J. N., "Hypersonic Viscous Shock-Layer Solutions over Long Slender Bodies—Part II: Low Reynolds Number Flows," *Journal of Spacecraft and Rockets*, Vol. 27, No. 2, 1990, pp. 185–193.

[25]Lee, K. P., and Gupta, R. N., "Viscous-Shock-Layer Analysis of Hypersonic Flows," NASA CR-189614, March 1992.

[26]Sakamura, Y., and Nishida, M., "Numerical Calculation of Thermal and Chemical Nonequilibrium Flows Around a Hypersonic Reentry Vehicle," *Transactions of the Japan Society for Aeronautical and Space Sciences*, Vol. 34, No. 103, May 1991, pp. 27–45.

[27]Akey, N. D., and Cross, A. E., "Radio Blackout Alleviation and Plasma Diagnostic Results from a 25,000 Foot Per Second Blunt-Body Reentry," NASA TN D-5615, Feb. 1970.

[28]Granthan, W. L., "Flight Results of 25,000 Foot Per Second Reentry Experiment Using Microwave Reflectometers to Measure Plasma Electron Density and Standoff Distance," NASA TN D-6062, Dec. 1970.

[29]Jones, W. L., Jr., and Cross, A. E., "Electrostatic Probe Measurements of Plasma Parameters for Two Reentry Flight Experiments at 25000 Feet Per Second," NASA TN D-6617, April 1972.

[30]Gnoffo, P. A., "Code Calibration Program in Support of the Aeroassisted Flight Experiment," *Journal of Spacecraft and Rockets*, Vol. 27, No. 2, pp. 131–142.

[31]Dunn, M. G., and Kang, S. W., "Theoretical and Experimental Studies of Re-entry Plasmas," NASA CR-2232, April 1993.

[32]Cauchon, D. L., "Radiative Heating Results from the FIRE II Flight Experiment at a Reentry Velocity of 11.4 Kilometers Per Second," NASA TM X-1402, July 1967.

[33]Gupta, R. N., "Navier-Stokes and Viscous Shock-Layer Solutions for Radiating Hypersonic Flows," AIAA Paper 87-1576, June 1987.

[34]Zoby, E. V., and Sullivan, E. M., "Effects of Corner Radius on Stagnation-Point Velocity Gradients on Blunt, Axisymmetric Bodies," NASA TM X-1067, March 1965.

[35]Hartung, L. C., "Development of a Nonequilibrium Radiative Heating Prediction Method for Coupled Flowfield Solutions," *Journal of Thermophysics and Heat Transfer*, Vol. 6, No. 4, 1992, pp. 618–625.

[36]Zoby, E. V., "Approximate Heating Analysis for the Windward-Symmetry Plane of Shuttle-Like Bodies at Large Angle of Attack," AIAA Paper 81-1042, June 1981.

[37]Zoby, E. V., Gupta, R. N., and Simmonds, A. L., *Temperature-Dependent Reaction Rate Expressions for Oxygen Recombination*, edited by H. F. Nelson, Vol. 96, Progress in Aeronautics and Astronautics, AIAA, New York, 1985, pp. 445–464.

[38]Goldstein, H., "Reusable Thermal Protection System Development—A Perspective," NASA CP-3157, Feb. 1992.

[39]Gupta, R. N., Lee, K. P., and Zoby, E. V., "Enhancements to Viscous-Shock-Layer Technique," *Journal of Spacecraft and Rockets*, Vol. 30, No. 4, 1993, pp. 404–413.